Sound wave propagation on the human skull surface with bone conduction stimulation

Dobrev, Ivo ; Sim, J H ; Stenfelt, Stefan ; Ihrle, Sebastian ; Gerig, Rahel ; Pfiffner, Flurin ; Eiber, Albrecht ; Huber, A M ; Röösli, Christof

DOI: https://doi.org/10.1016/j.heares.2017.07.005

Accepted Manuscript

Sound wave propagation on the human skull surface with bone conduction stimulation

Ivo Dobrev, Jae Hoon Sim, Stefan Stenfelt, Sebastian Ihrle, Rahel Gerig, Flurin Pfiffner, Albrecht Eiber, Alexander M. Huber, Christof Röösli

PII: S0378-5955(17)30258-7

DOI: 10.1016/j.heares.2017.07.005

Reference: HEARES 7396

To appear in: *Hearing Research*

Received Date: 1 June 2017

Revised Date: 5 July 2017

Accepted Date: 13 July 2017

Please cite this article as: Dobrev, I., Sim, J.H., Stenfelt, S., Ihrle, S., Gerig, R., Pfiffner, F., Eiber, A., Huber, A.M., Röösli, C., Sound wave propagation on the human skull surface with bone conduction stimulation, *Hearing Research* (2017), doi: 10.1016/j.heares.2017.07.005.

Sound wave propagation on the human skull surface with bone conduction stimulation

Ivo Dobrev, PhD[1,2], Jae Hoon Sim, PhD [1,2], Stefan Stenfelt, PhD [3], Sebastian Ihrle, Dr.-Ing[4], Rahel Gerig, PhD[1,2], Flurin Pfiffner, PhD[1,2], Albrecht Eiber, Dr.-Ing. [4], Alexander M. Huber, MD[1,2], Christof Röösli, MD[1,2]

[1]Department of Otorhinolaryngology, Head and Neck Surgery, University Hospital Zürich, Switzerland

[2] University of Zürich, Zürich, Switzerland

[3] Department of clinical and experimental medicine, Linköping University, Linköping, Sweden

[4] University of Stuttgart, Stuttgart, Germany

Corresponding Author:
Ivo Dobrev, PhD
Department of Otorhinolaryngology, Head and Neck Surgery, University Hospital Zurich
Frauenklinikstrasse 24
CH-8091 Zurich, Switzerland
E-Mail: ivo.dobrev@usz.ch
Phone: 0041 44 255 1111

Abstract

Background: Bone conduction (BC) is an alternative to air conduction to stimulate the inner ear. In general, the stimulation for BC occurs on a specific location directly on the skull bone or through the skin covering the skull bone. The stimulation propagates to the ipsilateral and contralateral cochlea, mainly via the skull bone and possibly via other skull contents. This study aims to investigate the wave propagation on the surface of the skull bone during BC stimulation at the forehead and at ipsilateral mastoid.

Methods: Measurements were performed in five human cadaveric whole heads. The electro-magnetic transducer from a BCHA (bone conducting hearing aid), a Baha® Cordelle II transducer in particular, was attached to a percutaneously implanted screw or positioned with a 5-Newton steel headband at the mastoid and forehead. The Baha transducer was driven directly with single tone signals in the frequency range of 0.25 – 8 kHz, while skull bone vibrations were measured at multiple points on the skull using a scanning laser Doppler vibrometer (SLDV) system and a 3D LDV system. The 3D velocity components, defined by the 3D LDV measurement coordinate system, have been transformed into tangent (in-plane) and normal (out-of-plane) components in a local intrinsic coordinate system at each measurement point, which is based on the cadaver head's shape, estimated by the spatial locations of all measurement points.

Results: Rigid-body-like motion was dominant at low frequencies below 1 kHz, and clear transverse traveling waves were observed at high frequencies above 2 kHz for both measurement systems. The surface waves propagation speeds were approximately 450 m/s at 8 kHz, corresponding trans-cranial time interval of 0.4 ms. The 3D velocity measurements confirmed the complex space and frequency dependent response of the cadaver heads indicated by the 1D data from the SLDV system. Comparison between the tangent and normal motion components, extracted by transforming the 3D velocity components into a local coordinate system, indicates that the normal component, with spatially varying phase, is dominant above 2 kHz, consistent with local bending vibration modes and traveling surface waves.

Conclusion: Both SLDV and 3D LDV data indicate that sound transmission in the skull bone causes rigid-body-like motion at low frequencies whereas transverse deformations

and travelling waves were observed above 2 kHz, with propagation speeds of approximately of 450 m/s at 8 kHz.

Keywords: bone conduction, 3D Laser Doppler Vibrometry, wave propagation, rigid body motion, transverse deformation, full-field measurements, human cadaver head

1 Introduction

Bone conduction hearing aids (BCHAs) have become a widely used tools in hearing rehabilitation for patients with conductive or mixed hearing loss (i.e. ear atresia, or chronic inflammation with discharge) who cannot wear conventional hearing aids. Another indication for BCHAs is patients with single-sided deafness (SSD). The aim of BCHAs in this situation is to route sound from the deaf side to the hearing side. The efficacy of the sound propagation in BC hearing, from the BCHA to the target ear, depends of several important aspects.

First, the propagation path of the sound energy could involve several possible pathways, through which sound reaches and stimulates the cochlea. Most authors agree that these pathways and their interactions depend on frequency and on the state of the middle ear ossicles (Stenfelt, 2006; Stenfelt and Goode, 2005 (a); Tonndorf, 1966; Stenfelt, 2016). The following pathways have been identified: a) pathways involving bone vibration resulting in compression and expansion of the otic capsule (Stenfelt, 2014; Tonndorf, 1966; von Bekesy, 1960); b) sound radiated in the external auditory canal (Brummund et al., 2014; Stenfelt et al., 2003); c) inertia of the ossicles (Homma et al., 2010; Stenfelt, 2006; Stenfelt et al., 2002); d) inertia of the inner ear fluid (Kim et al., 2011; Stenfelt, 2014). e) non-osseous pathway including sound pressure transmission by the contents of the skull, such as brain tissue and cerebrospinal fluid via the internal auditory canal, cochlear aqueduct and/or vestibular aqueduct to the cochlea (Sohmer and Freeman, 2004; Sohmer et al., 2000; Sim et al. 2016; Röösli et al. 2016).

Second, the site of stimulation influences the perception. The closer the BCHA is placed to the cochlea, the more efficient the stimulation is (Eeg-Olofsson et al., 2011). For patients with SSD, stimulation occurs at the contralateral ear and sound propagates across the head, via one of the above-mentioned pathways, to finally stimulate the ipsilateral cochlea. The loss of sensitivity between ipsilateral and contralateral stimulation is called transcranial attenuation. Clinically, transcranial attenuation is important because it defines the amount of masking necessary for measuring monaural BC thresholds (Hood, 1960; Studebaker, 1964). However, it varies considerably between individuals ranging from 0 to 15dB between 0.25 to 4 kHz (Hurley and Berger,

1970; Snyder, 1973; Nolan and Lyon, 1981). Further, it has been shown that stimulation superior-anterior to the pinna is more efficient than behind the pinna even with the same distance from the cochlea (Dobrev et al., 2016; Ito et al, 2011).

For patients with SSD, where sound from a BCHA mounted contralaterally have to stimulate the ipsilateral cochlea, four different mechanism of sound propagation are possible; waves a) tangential and b) normal to the skull bone surface, c) rigid body motion, and d) direct propagation through cerebrospinal fluid and brain tissue. Knowledge about how sound reaches the contralateral ear is important for patients with SSD using BCHA as the device should be designed and implanted (or worn) to minimize inter-aural attenuation and resulting in maximum amplification. However, for patients with bilateral BCHA, large transcranial attenuation is desired because it may be beneficial for binaural hearing (Stenfelt, 2012; Håkansson et al. 2010).

The aim of this study is to investigate the mode of transcranial sound propagation for BC stimulation. Our hypothesis is that the mode of sound propagation is frequency dependent, and that a transversal wave is dominant at high frequencies (>1 kHz).

2 Methods

This study was approved by the Ethical Committee of Zurich (KEK-ZH-Nr. 2012-0136).

2.1 Sample preparation

Five Thiel-fixed (Thiel, 1992) adult cadaver heads were used. The intracranial space was filled with water and remnants of brain. To maintain the pressure level of the intra-cranial fluid in the cadaver head similar to the physiological condition, a tube was attached to the skull through a hole at the superior center, and the water column inside the tube was controlled to have a height of 15 cm (Steiner and Andrews, 2006). The heads were positioned such that the posterior part of the skull was supported by a soft gel head ring (Model 4006.0200, MAQUET Medical Systems, USA), positioned on a stainless-steel table to decouple vibrations from external sources.

2.2 Measurement setup

The electro-magnetic transducer from a BCHA (bone conduction hearing aid), a Baha® Cordelle II transducer (Cochlear, Australia) in particular (referred to as simply Baha or Baha transducer), was used for stimulation. In order to compare the response of the skull at multiple excitation conditions and locations, the effective stimulation force from the transducer in each condition needed to be calibrated. The dynamic stimulation forces acting on the skin (stimulation with the steel headband) were estimated using an artificial mastoid Type 4930 (Brüel and Kjær, Denmark). The stimulation forces acting on the screw attached to the skull was calibrated using a skull simulator (TU-1000, Cochlear Bone Anchored Solutions AB, Sweden).

The Baha transducer was placed either at its typical location on the mastoid, 5 cm behind the opening of the external auditory canal, or at the forehead, in the midline 5 cm above the root of the nose. The Baha was attached to the head either using a 5-Newton steel-headband (Baha headband 90138, Cochlear AG, Australia) or screw implanted in the bone. The Baha transducer was driven directly by single tone stimuli, of 10 V peak in the frequency range of 0.25 – 8 kHz. For measurements with the 1D scanning laser Doppler vibrometer (SLDV), the velocity signal from the skull response and the driving signal to the BC transducer are generated and recorded at 25.6kHz with a NI PCI-4461 (National Instruments Corp., USA) integrated within a PSVW401-B data acquisition system, controlled via PSV 9.0 software (Polytec GmbH, Germany). Due to timing constrains, the 1D LDV recording was done with 40 ms sampling time (25 Hz frequency resolution), repeated and averaged in the complex domain 10 times. For the 3-dimentional laser Doppler vibrometer (3D LDV) measurements, the velocity and the driving signals are recorded and generated with DS 2102 DAC and DS 2004 ADC boards, respectively, integrated within a dSpace DS1006 data acquisition system (dSpace, Germany), controlled via custom made MATLAB script (MathWorks, Natick, MA, USA). The 3D LDV recording was done with 80 ms sampling time (12.5 Hz frequency resolution), repeated and averaged in the complex domain 15 times. An overview of the block diagram of the measurement system is presented in Figure 1A, with corresponding sampling points grid, shown in Figure 1B.

Noise floor measurements were conducted for each experimental configuration by not providing a signal to the BC transducer, while keeping the corresponding experimental configuration unchanged. Data with signal-to-noise ratio (SNR) below 10 dB was discarded. Additional signal quality check was done based on the signal coherence between the velocity signal(s) for each LDV and the corresponding stimulus signal. Coherence varied from 1 (for ideal coherence between the response velocity and stimulation signal at the excitation frequency) and 0 for no coherence, and data with coherence below 0.85 was discarded in further processing steps. Since the response at each frequency is recorded individually, discarding one measurement results in discarding only one of the full set of measurement frequencies, but not the whole set. The coherence calculations for the LDV measurements were done based on the complex frequency spectrum of the velocity and stimulus signals, as defined in the PSV 9.0 software (Polytec GmbH, Germany).

One-dimensional motions, with sensitivity along the optical axis, of the surface of the skull were measured by a SLDV (OFV-3001, Polytec GmbH, Waldbronn, Germany) system at approximately 400 points in 20×20 grid at 5 mm square pitch, evenly distributed across the superior area of the skull. The full 3-dimensional motion response of the same area was also measured with a 3D LDV (CLV-3D, Polytec GmbH, Waldbronn, Germany) at approximately 20 points in a 4×5 grid at 25 mm square pitch. The measurement point position of the SLDV was controlled via 2-axis scanning unit (OFV 040, Polytec GmbH, Waldbronn, Germany), and the distance between the SLDV and the measurement surface was set to approximately 1m, which reduces the difference in motion sensitivity direction due to variation in orientation (< ±3°for a 10x10 cm measurement area) of the laser beam between measurement points. The measurement position of the 3D LDV was controlled via a custom made 3-axis positioner, which maintained identical orientation of the measurement coordinate system between points.

For measurements with both LDV system types, the Z-axis was defined along the LDV optical axis oriented along the superior-inferior direction (normal to the viewing plane of the LDV camera), while the X- and Y-axis where oriented along the lateral-medial (left-right) and anterior-posterior directions (horizontal and vertical, in viewing

plane of the LDV camera), respectively, as shown in Figure 2A. The measurement area covered the superior section of the scull, approximately ~100×100mm. Table 1 gives an overview over the measurements done on each head. Due to time and availability constraints, not all measurements were done on each head. In general, measurements where done in two major stages. In the first stage, 1D velocity data with high spatial resolution (~5mm pitch), measured with the 1D SLDV, was obtained from 3 heads (head 1-3). In the second stage, velocity data with lower spatial resolution (~25mm pitch) but along all 3 orthogonal directions, measured with the 3D LDV, was obtained from 2 heads (head 4 and 5), where for head 4 three different surface conditions were measured.

2.3 Surface wave propagation speed calculation

The propagation speed of the surface waves, v_{wave}, was estimated based on the period time, T_{cycle}, of the excitation signal, and the wavelength, λ, defined as the circumferential distance between two neighboring nodes, along the propagation direction, in the phase map as follows:

$$v_{wave} = \frac{\lambda}{T_{cycle}} = \frac{r\theta}{T_{cycle}} = \frac{2r[arcsin(a/2r)]}{T_{cycle}} \quad (1)$$

, where a is the straight line distance (projected onto the viewing plane of the LDV camera) between two neighboring nodes in the wave pattern, and r is the approximate radius of the skull (approximated as a sphere). Note that θ, the angle corresponding to the arc length λ, is in radians. An example phase map, depicting a typical wave pattern of skull vibration at 8 kHz, and the corresponding graphical definition of the aforementioned parameters are shown in Figure 2 A and B.

2.4 Intrinsic coordinate system at each measurement point

While the data from the 3D LDV completely defines the motion of each measurement point, the measurement (LDV) coordinate system is oriented somewhat arbitrary to the skull surface. In order to define the data in an anatomically relevant coordinate system, the local surface normal and tangents at each measurement point has been chosen to define a local intrinsic coordinate system (Khaleghi et al., 2015). This provides the means to express the velocity in terms of tangential and normal components, which directly describe the longitudinal (in-plane deformation) and transverse (our-of-plane deformation) motion locally, at each measurement point on the skull surface.

Figure 2C illustrates the relation between the two measurement systems used in this work: 1) the measurement (LDV) coordinate system, defined by the $\hat{X}$, $\hat{Y}$ (perpendicular to the LDV optical axis) and $\hat{Z}$ (along the LDV optical axis) unit vectors, oriented along the X, Y and Z axes, respectively ; and 2) the intrinsic (local, anatomical) coordinate system, defined by the $\hat{\eta}$ (surface normal), $\hat{t}$ (1st surface tangent component) and $\hat{b}$ (2nd surface tangent component) unit vectors, along the η, t and b axes, respectively (see Figure 2 A and C). The two surface tangent unit vectors $\hat{t}$ and $\hat{b}$ lie on a plane tangential to the skull surface at each measurement point. The spatial transformation from the measurement to intrinsic coordinate system can be defined with a single rotation matrix using two pieces of information: 1) the angle α between the $\hat{\mathrm{Z}}$ and $\hat{\eta}$ unit vectors, defined as the $arccos$ of their dot product (assuming α <90deg, where α = 90deg corresponds to the LDV laser beam being parallel to the measurement surface); and 2) the unit vector, $\hat{\mathrm{K}}$, of the axis of rotation, defined as the cross product between the $\hat{\mathrm{Z}}$ and $\hat{\eta}$ unit vectors (Khaleghi et al., 2015). This information is sufficient to uniquely define and apply the Rodrigues' rotation formula (Rodriguez, 1840), which defines a rotational matrix around an arbitrary axis of rotation.

The surface normal unit vector, $\hat{\eta}$, unique for each measurement point, is obtained from the shape of the skull, which in turn is approximated by fitting a 2-D surface (using 2nd order 2 variable polynomials) to the point cloud, representing the measurement

points' positions. The fitting was done using the MATLAB function "fit" (MATLAB 2016a, MathWorks, Natick, MA, USA).

Within the rest of this work, the motion components of the intrinsic (local) coordinate system are referred to as follows: the motion component along the surface normal unit vector $\hat{\eta}$ is referred to as "normal" component or V_η component; the motion components along the unit vectors of the surface tangents, $\hat{t}$, and $\hat{b}$, are referred to as "tangent" components when referred to collectively, or as V_t and V_b components, when referred to individually; the motion components of the LDV (measurement) coordinate system are referred to as V_X, V_Y, and V_Z components. The orientations of the two tangent unit vectors $\hat{t}$ and $\hat{b}$, as defined by within this work, are not related to the traditionally defined surface tangent and binormal, which are oriented in the direction of highest slope of the measurement surface at the measurement point. Within the context of this work, the direction of the surface tangent unit vectors $\hat{t}$ and $\hat{b}$ is solely defined by the direction of the surface normal relative to the optical axis of the measurement system. However, for the purpose of the discussions within this work, the specific orientations of $\hat{t}$ and $\hat{b}$ unit vectors are ignored, as the individual contribution of the corresponding motion components V_t and V_b is not of interest but only the magnitude of their collective contribution, expressed as the combined surface tangent motion component V_T (defined in section 2.6).

2.5 Rigid body motion fit

The bone conduction induced motion at each point of a cadaver head can be approximated as a combination of two spatial "modes" of vibration (Stenfelt, 2011): 1) a pure rigid body motion (RBM), representing the bulk spatial motion of the whole head, with no relative motion (deformation) between individual points; and 2) motion resulting in local deformation, due to relative motion between individual points of the skull bone. In order to differentiate between the two, we estimated the amount of difference between the measured motion at each point and the predicted motion based on pure RBM of the whole head. The RBM was estimated as a mathematical fitting of the measured motions of all points. The mathematical fitting was based on the relation

between the RBM, expressed as a 6-component (3 translational and 3 rotational components) velocity vector $\mathbf{v}_r$, and the motion of single point, expressed as a 3-component (3 translational components) velocity vector v_m, defined as follows (Sim et al., 2010):

$$\mathrm{v}_m = \mathrm{B}_m \mathbf{v}_r \tag{2}$$

with $\mathrm{B}_m = \begin{bmatrix} 1 & 0 & 0 & 0 & \mathrm{z_m} & -\mathrm{y_m} \\ 0 & 1 & 0 & -\mathrm{z_m} & 0 & \mathrm{x_m} \\ 0 & 0 & 1 & \mathrm{y_m} & -\mathrm{x_m} & 0 \end{bmatrix}$ and $\mathbf{v}_r = \begin{Bmatrix} \mathbf{v}_o \\ \boldsymbol{\omega} \end{Bmatrix} = \begin{Bmatrix} \mathrm{v}_{ox} \\ \mathrm{v}_{oy} \\ \mathrm{v}_{oz} \\ \omega_x \\ \omega_y \\ \omega_z \end{Bmatrix}$,

where $\mathbf{v}_o$ and $\boldsymbol{\omega}$ indicate vectors for the translational and the rotational velocity of the rigid body (specifically the origin point o), and $(\mathrm{x_m}, \mathrm{y_m}, \mathrm{z_m})$ are the coordinates of the point *m* in the measurement frame. To determine the six rigid-body motion components, at least three non-collinear points need to be measured. Since the measurements of the vibrational motion were performed at ~20 points with the 3D LDV system and ~300-400 points with the SLDV system, Eq. 2 is used to set an over-defined system of equations, which can be solved for the vector $\mathbf{v}_r$ by the method of least squares error as:

$$\mathbf{v}_r = (\mathbf{A}^{\mathrm{T}}\mathbf{A})^{-1}(\mathbf{A}^{\mathrm{T}}\mathbf{v}_{\mathrm{M}}) \tag{3}$$

with $\mathbf{v}_{\mathrm{M}} = \begin{Bmatrix} (\mathrm{v}_1)_{\mathrm{m}} \\ (\mathrm{v}_2)_{\mathrm{m}} \\ \dots \\ (\mathrm{v}_n)_{\mathrm{m}} \end{Bmatrix}$, and $\mathbf{A} = \begin{Bmatrix} (\mathrm{B}_1)_{\mathrm{m}} \\ (\mathrm{B}_2)_{\mathrm{m}} \\ \dots \\ (\mathrm{B}_n)_{\mathrm{m}} \end{Bmatrix}$.

Once $\mathbf{v}_r$ is calculated from Eq. 3, it can be plugged back into Eq. 2 giving a predicted motion v'_m of each point, based on the RBM fit, $\mathbf{v}_r$. The difference between the predicted (calculated) motion, v'_m, and measured motion v_m can be then calculated at each point.

While the 3D LDV measurements provides all 3 motion components (V_X, V_Y, and V_Z) at each measurement point, the SLDV system provides only 1 motion component (V_Z). The 1D data of the SLDV can be still used for the partial calculation of the RBM $\mathbf{v}_r$, defining only one translational component v_{oz} (motion along the Z axis of the measurement system) and 2 rotational components ω_x and ω_y (rotation around the X

and Y axes of the measurement system), based on Eq. 3. Similarly, Eq. 2 produces a predicted (calculated) motion, $\mathrm{v'}_m$, with only one translational component along the Z axis of the measurement system.

The average difference, across measurement points, between the calculated "pure" rigid body motion and the measured motion, is used as a metric to approximate the extent to which the cadaver head undergoes pure rigid body motion only, or local deformation as well. This average difference is normalized to the average motion of all points, in order to scale its significance relative to the observed motion. The normalized average RBM difference, $\Delta\mathrm{v}_r$, can be expressed as:

$$\Delta\mathrm{v}_r = \left[\frac{|\Delta\mathbf{V}_m|}{|\overline{\mathbf{V}_m}|}\right] = \left[\frac{|\langle\mathrm{v}_m - \mathrm{v'}_m\rangle|}{|\langle\mathrm{v}_m\rangle|}\right] \quad (4)$$

In the numerator, $\Delta\mathbf{V}_m$ is the combined spatial vector (based on Eq. 8, Section 2.7) of the vector difference between the measured velocity, v_m, and predicted $\mathrm{v'}_m$ velocity at each point m, reversely calculated based on the rigid body motion $\mathbf{v}_r$. In the denominator, $\mathbf{V}_m$ is combined spatial vector, based on Eq. 8, of the measured velocity v_m at each point m. The operator $\overline{A_\iota}$ indicates the geometric mean of the set of n numbers $A_{i,i=1..n}$, the operator $|A|$ indicates the magnitude of the complex number A, and the operator $\langle A\rangle$ indicates the combined spatial motion vector of the 3-element velocity vector A. Based on these definitions, it should be noted that while v_m and $\mathrm{v'}_m$ are 3-element vectors (each element is a complex number), the numerator and denominator are positive real numbers, and so is $\Delta\mathrm{v}_r$. In the case of 1D data from the SLDV system, v_m and $\mathrm{v'}_m$ have only a single velocity component (i.e., V_z), making the conversion to spatial vectors (via the operator $\langle A\rangle$) redundant and is thus omitted.

A value of $\Delta\mathrm{v}_r$ close to or above 1 (0 or positive values in dB scale) would indicate a significant difference between the estimated rigid body motion $\mathbf{v}_r$ and the measured velocity v_m at all points. A value of $\Delta\mathrm{v}_r$ sufficiently smaller than 1 (negative values in dB scale), would indicate a close fit between the estimated rigid body motion $\mathbf{v}_r$ and the measured velocities v_m at all points.

2.6 Combined spatial motion vector

Since the 3D LDV provides all 3 Cartesian componets of the motion at each measurement location, the magnitude and phase of the total (combined) motion, $\boldsymbol{V}$, was calculated as the sum of the ortogonal vectors, V_x, V_y, and V_z, representing the 3 measured motion components, as follows:

$$\boldsymbol{V}(t) = V(t)\boldsymbol{n}(t) = V_x(t)\boldsymbol{i} + V_y(t)\boldsymbol{j} + V_z(t)\boldsymbol{k} \quad (5)$$

, where $\boldsymbol{n}$ is the instantaneous spatial unit vector of $\boldsymbol{V}$ (representing the instantaneous spatial direction of motion), and V is the instantaneous magnitude of $\boldsymbol{V}$ (representing the instantaneous speed). The unit vectors $\boldsymbol{i}$, $\boldsymbol{j}$, and $\boldsymbol{k}$ are in the X, Y, and Z axes in measurement (LDV) coordinate system, but can also equally represent the unit vectors in the η, t, and b axes, corresponding to V_η, V_t, and V_b motion components defined in intrinsic (local, anatomical) coordinate system. In this case, the $\boldsymbol{V}$, V, $\boldsymbol{n}$ remain unchanged, as they are defined by the motion at each measurement point and not by the choice of coordinate system. The parameters $\boldsymbol{V}$, V, $\boldsymbol{n}$, V_X, V_Y, and V_Z are a function of time and have their corresponding magnitude and phase. Assuming that the measured motion is harmonic, the Cartesian motion components, V_i, where $i = X, Y, Z$ for measurement coordinate system ($i = \eta, t, b$ for intrinsic coordinate system), can be expressed as a function of an angular frequency, ω, time, t, and phases θ_X, θ_Y, and θ_Z, respectively, as follows:

$$V_i(t) = |V_i| \cos(\omega t + \theta_i) \quad (6)$$

Using Eqs. (5) and (6), the instantaneous magnitude, V, of the combined spatial vector can be expressed as:

$$V^2 = V(t)^2 = \sum_{i=X,Y,Z} |V_i|^2 \cos^2(\omega t + \theta_i) \quad (7)$$

Eq. (7) can be transform in the final form:

$$V(t)^2 = \frac{1}{2}\left[\sum_{i=X,Y,Z} |V_i|^2 + \sqrt{A^2 + B^2}cos(2\omega t + 2\theta)\right]^2 \quad (8)$$

where:

$$A = \sum_{i=X,Y,Z} |V_i|^2 \cos(2\theta_i)$$

$$B = \sum_{i=X,Y,Z} |V_i|^2 \sin(2\theta_i) \quad (9)$$

$$\tan(2\theta) = \frac{B}{A}$$

Based on Eq. (8) it should be noted that, even though the instantaneous magnitude of each of the individual Cartesian components becomes zero during a vibration cycle, the magnitude, V, of the combined spatial vector $\boldsymbol{V}$ does not, unless the phases θ_x, θ_y, and θ_z are the same or have multiples of π difference between each other.

Equations 5 - 9 can be applied in analogues manner in the intrinsic coordinate system (defined in Section 2.4), with the 3 orthogonal velocity components consisting of a normal and two tangent velocity components. While the directions of the tangent components are defined uniquely at each point, their orientation in the tangent plane at each point could vary between points. However, in order to establish the contribution of the tangent velocity components relative to the normal velocity component, the individual contributions from the V_t and V_b components are disregarded, and only the contribution from their combined motion, V_T, is considered. The instantaneous magnitude of the combined tangential motion, V_T, is calculated by plugging the two tangential components, V_t and V_b, into the Eq. 8, while omitting the 3rd motion component.

3 Results

3.1 Force calibration for implant and steel headband attachment

In order to study the response of the cadaver heads to different excitation conditions (location, attachment type), while accounting for differences in the force output level of the Baha under each corresponding condition, all velocity measurements have been normalized to the corresponding estimated output force from the Baha transducer. This required the estimation of the Baha impedance for each of the two attachment conditions used throughout our measurements: 1) Baha attached transcutaneously to the skull via a screw implant; 2) Baha held against the skin via a 5-Newton steel-headband.

The frequency dependence of the force output per unit of driving voltage of the Baha transducer, for stimulation via a steel headband, was calibrated on an artificial mastoid, which in turn conformed to the IEC 60318-6:2007 standard. The mechanical impedance of the artificial mastoid was calibrated with a shaker and impedance head (Type 4810 and 8000, respectively, Brüel and Kjær, Denmark). The frequency dependence of the force output of the Baha transducer, for stimulation via an implant (screw), was calibrated via a skull simulator (TU-1000, Cochlear Bone Anchored Solutions AB, Sweden), with a calibration curve of the skull simulator provided by the manufacturer. Note that these calibration methods account for only the one of the six components of the force output of the Baha transducer, namely a force normal to the attachment surface. The effects of the other 5 components (2 tangential forces and 3 torsional moments) produced by the Baha transducer are assumed to be negligible. Additionally, these calibration methods do not account for possible effects on the Baha force output due to local point impedance variations across different stimulation points on the skull (Stenfelt and Goode, 2005 (a)).

Figure 3 shows comparison between the force output (both magnitude and phase) of the Baha transducer when supported via an implant (screw) and steel headband. The responses are similar (within 5dB) at low frequencies (below 400 Hz), however, the implant attachment condition allows for higher (10-20 dB) force output per unit of excitation voltage at higher frequencies, particularly above 2 kHz. Both attachment conditions provide similar phase delay between input voltage and output force, with an

396 average slope of 0.5 cycle/decade, with higher slopes around the first natural frequency
397 of the transducer at each attachment condition, namely 420 Hz for steel headband and
398 550 Hz for implant support.
399

400 3.2 Surface wave propagation

401 Figure 4 shows magnitude and phase maps of the velocity of the surface of the
402 skin or skull in three cadaver heads (bare skull in Head 1, and skin covered skulls in
403 Head 2 and 3) stimulated via the Baha transducer, attached via an implant anchored at
404 the mastoid. Such high spatial resolution (~5mm pitch) data was obtain only for head 1-
405 3, but not for 4-5. The velocities have been normalized by the force response of Baha
406 transducer, as shown in Figure 3. Spatial gradients of the phase map data indicate the
407 gradual transition from rigid-body vibration at low frequencies (below 1 kHz) to traveling
408 waves at higher frequencies (above 2 kHz). Based on the phase maps at 6-8 kHz, and
409 methods explained in Section 2.3., the speed of wave propagation is estimated in the
410 range of 450-500 m/s, based on data from heads 1-3.
411 The spatial pattern distribution of both the magnitude and phase maps changes
412 from simple, with only 2 local maxima within the recorded area (~10×10cm), at low
413 frequencies (below 1 kHz), to more complex one with multiple (>5-10) local maxima at
414 higher frequencies. Based on a representative RBM fit for Head 3 (last column of figure
415 3), the average difference between RBM fit and measured data is small ($\Delta \mathrm{v}_r < 10\ dB$)
416 relative to the average measured motion at low frequencies (0.5-1kHz), indicating a
417 predominantly rigid-body-like motion pattern. This is confirmed through comparison
418 between the measured and RBM estimated motion of Head 3, indicating qualitative
419 similarities in the spatial distribution of the magnitude and phase maps at 0.5 kHz. At
420 higher frequencies (6-8 kHz) the RBM fit error increases to approximately ($\Delta \mathrm{v}_r \approx 0\ dB$)
421 as much as the average measured motion itself, and the motion phase pattern indicates
422 local transverse deformation with travelling waves. The traveling waves originate from
423 the stimulation point (marked with a dot in the last row of figure 4) and propagate
424 contra-laterally, as indicated by arrows in the bottom row of figure 4.
425

3.3 Implant vs. headband stimulation at mastoid and forehead

The motions of the skull for stimulation at the mastoid, with Baha transducer attached via either headband or screw, are displayed in figure 5 for 0.5, 2 and 8 kHz. The spatial distribution of the magnitude and phase patterns are similar with lower (5-10dB) magnitude levels for the screw attachment. This indicates that stimulation on the skin results in a similar wave propagation pattern as stimulation directly on the bone. The average RBM fit difference Δv_r is approximately -9dB at low frequencies and 0dB at high frequencies, relative to the corresponding average measured motion.

Figure 6 shows the magnitude and phase maps of the vibration response of the skin surface covering the skull of Head 2, with Baha stimulation at the forehead via either headband or screw attachment. In both attachment conditions, rigid-body-like motions, with an average normalized RBM fit difference Δv_r of approximately -8 to -7 dB, were dominant at low frequencies, below 1 kHz, while local transverse (approximately normal to the skull surface) deformation patterns with traveling waves were observed at high frequencies, above 2 kHz. A complex motion was observed between 1 – 2 kHz possibly consisting of a mixture of motion modes. Similar to the case of mastoid stimulation (Figure 5), the spatial pattern of both magnitude and phase maps changes from simple, with only 1-2 local maxima within the measurement area (~10×10cm), at low frequencies (below 1 kHz), to a more complex pattern (> 3 maxima) above 2 kHz. However, both the magnitude and phase patterns for stimulation of the forehead are rotated 90-120 degrees relative to the corresponding data for stimulation on the mastoid, which is consistent with the change in excitation position. Travelling wave patterns at high frequencies are also similar in spatial pattern for the two stimulation positions, however direction of propagation is from anterior to posterior, for forehead stimulation, as opposed to ipsi- to contra-lateral, for mastoid stimulation. In general, the direction of the travelling waves was along the circumference passing through he stimulation point.

3.4 3D motion components of surface wave propagation

The 3D motion components of the surface wave propagation were measured for stimulation on the mastoid with the Baha actuator attached to a screw anchored in the skull in two heads. Measurements were done directly on the skulls surface by removing the skin on and around the measurement area. A total of 15-20 points were measured resulting in a reduced spatial resolution (25 mm vs. 5 mm pitch) compared to the 1D SLDV data.

Figure 7 shows the magnitude and phase of the V_X, V_Y, and V_Z components of the velocity data in LDV coordinate system, as well as the normal and combined tangent (see section 2.6 for definition) components, V_η and V_T, in the intrinsic (local) coordinate system.

The motion pattern at low frequency (250Hz) indicates an average V_X magnitude approximately 10 dB higher than V_Y, and V_Z components in LDV coordinate system. This is consistent with a combined tangent component V_T being 10 dB higher than the normal component V_η and the same frequency. The approximately uniform spatial distribution of both phase (spatial slopes of 5-10 deg/cm) and magnitude (3-5 dB variation across the measurement area) of V_T and V_X, indicate predominant (Δv_r = -16dB) rigid-body-like motion consisting of translational motion directed approximately along the X-axis of LDV coordinate system (left-right relative to the cadaver head), coinciding with the direction of excitation of the Baha. The slight spatial variation in both magnitude and phase could be explained by considerable rotational components around the Y and Z axis indicated by the RBM fit.

The motion pattern at high frequencies (4 kHz) has a predominant (5-7 dB higher than other components) normal component, approximately oriented along the Z-axis in LDV coordinate system (out-of-plane relative to the figure plane). Spatial patterns show a non-uniform distribution for both phase (spatial slopes of 30-50 deg/cm) and magnitude (15-20 dB variation across the measurement area), indicating local deformations and traveling waves, emanating from the stimulation location and traveling circumferentially in contra-lateral direction. Estimated waves speeds are approximately 500-700m/s, consistent with estimations based on the 1D SLDV data. Differences in the

484 estimated waves speeds, based on the SLDV and 3D LDV data, could be attributed to
485 the lower spatial resolution of the 3D LDV data relative to the SLDV, possibly resulting
486 larger errors when estimating the wavelength. Overall, the measured magnitude and
487 phase maps (figures 4-6) are qualitatively comparable in spatial distribution between the
488 two velocity measurement methods.
489

490 3.5 Contribution from normal and tangent motion components

491 By averaging each motion component in the intrinsic frame (one combined tangent
492 and one normal component) across all points and normalizing it by the corresponding
493 average of the combined motion vector of all 3 components, the relative contribution of
494 each component is calculated, at each individual frequency, in figure 8 (left). The data in
495 figure 8 includes averaged (geometric mean) and individual data of measurements on
496 two heads, Head 4 and Head 5, where Head 4 is measured in 3 conditions: 1) intact
497 skin covering the skull; 2) skin is perforated (<5mm diameter) and exposing the bone at
498 the measurement points, while left intact in all other locations; and 3) skin is completely
499 removed from the skull within the measurement area (~10×10 cm). Data for Head 5
500 includes only the condition, where the skin is completely removed from the skull within
501 the measurement area. Additionally, figure 8 (right) includes the average normalized
502 RBM fit difference, $\Delta \mathrm{v}_r$ for each head (and corresponding skin condition) and
503 stimulation frequency, show as both individual and averaged (geometric mean) data.
504 Data in figure 8 (left) shows that at low frequencies (0.25-0.5 kHz) the combined
505 tangent component V_T is 5-15dB higher than the surface normal component V_η, while at
506 higher frequencies, their contribution is comparable with the surface normal V_η being 2-
507 5 dB larger. The transition between the two modes of motion happens at approximately
508 600-800Hz. Based on figure 8 (right), the low frequency (0.25-0.5 kHz) motion of the
509 measured skull surface could be approximated as RBM, with an average error 10-30dB
510 smaller than the averaged measured motion. However, at higher frequencies (above 2
511 kHz) the average RBM fit error becomes considerable, becoming within less than 5dB
512 of the average motion.
513

4 Discussion

4.1 Surface wave pattern and propagation speed

In principle, the spatial distribution of the velocity pattern, across the skull surface, could be a result of multiple vibration modes, each with a different wavelength, existing simultaneously at a single excitation frequency (McKnight et al., 2013). However, phase maps at high frequencies show consistent spatial periodicity in both direction and location, suggesting negligible effects of potential anisotropy of the skull structure or inhomogeneity in the bone's material properties.

At low frequencies (<1 kHz), surface velocity data in all cadaver heads, acquired with either the SLDV or the 3D LDV systems, indicate motion similar (in both magnitude and spatial distribution) to RBM (Δv_r from -30 to -10 dB), consistent with "mass-spring system" behavior previously reported in (Stenfelt and Goode, 2005 (a)). The 3D LDV system data indicate predominant longitudinal displacements (tangential to the skull surface), and no clear traveling wave patterns (Khalil et al., 1979; Håkansson et al., 1994).

At high frequencies (6-8 kHz), there are predominantly local transversal (normal to the skull surface) deformations (possibly bending) with traveling wave components, with estimated velocities of around 450-500m/s, starting at the Baha stimulation location and propagating along the skull surface circumference. The estimated propagation speeds correspond to a trans-cranial time interval of 0.4 ms at 8 kHz, consistent with previous observations (Stenfelt, S. and Goode, 2005 (b); Khalil et al., 1979; Håkansson et al., 1994; Tonndof and Jahn, 1981). In the mid frequency range (1-3 kHz) a complex motion was observed, possibly consisting of combination of both standing and traveling waves (Stenfelt and Goode, 2005 (a)).

4.2 Stimulation location and attachment type

Stimulation at either the mastoid or the forehead, with attachment via implant screw, produces comparable surface velocity, normalized by the excitation force, with similar spatial absolute values (within 5dB on average) and distribution of both magnitude and phase at each measurement frequency. Travelling wave patterns at high

frequencies (6-8kHz) are also qualitatively similar in spatial pattern, however direction of propagation is changed in accordance with the stimulation location.

In the case of forehead stimulation (figure 6), both screw and headband attachment type show qualitatively similar spatial distribution of the magnitude and phase maps at all frequencies. By accounting for the force output calibration of each attachment type, the absolute levels and ranges of the velocity response (admittance) are very similar (within 3-5 dB on average) at low (0.5 kHz) and mid frequencies (2 kHz), with larger differences (10-15 dB on average) at higher frequencies (8 kHz), in agreement with previous studies (Stenfelt and Håkansson, 1999). The deviations at higher frequencies could be explained by the attenuation of the mass-spring system that the skin and the headband form, which may not have been replicated sufficiently precise with the artificial mastoid calibration procedure. The variability of the input force of headband supported Baha at both the mastoid and the forehead, could potentially be reduced by a more accurate estimation of the input force and mechanical point impedance, individually for each head, attachment type and stimulation location, via direct measurements of the acceleration at the attachment point of the Baha and knowing the Baha transducer's effective moving mass, similar to (Stenfelt and Goode, 2005 (a)).

Regardless of the Baha attachment condition and stimulation location, the direction of propagation of the surface waves at high frequencies originated from the stimulation location and traveled circumferentially along the diameter, as can be seen with the phase patterns at high frequencies (8kHz) in Figures 5 and 6. While there were no visible traveling waves, but rather RBM-like displacements, the phase and magnitude distributions at lower frequencies (0.5kHz) were also affected by the stimulation location. This appears to cause the approximate alignment of the direction of the predominant spatial gradients, of both the magnitude and phase patterns, with a circumference passing through the stimulation location, similarly as the surface wave propagation direction at high frequencies.

While the analysis and observations of attachment method (headband vs. screw) and stimulation location (mastoid vs. forehead) were done on only head 2, due to time and resources constraints, we believe that these observations would hold for other

cadaver heads under similar conditions, because head 2 showed quantitatively similar wave propagation speeds and qualitatively similar motion patterns (based on qualitative comparison of the phase and magnitude maps in Fig. 4 and 7) as the other 4 heads under similar stimulation conditions.

4.3 3D motion response

Similar to the 1D motion data of the SLDV, the spatial distribution of all motion components (in both LDV and intrinsic coordinate systems, see Figure 7) recorded by the 3D LDV system, indicates rigid-body-like motion at low frequencies (< 1 kHz) and a spatially complex motion with local deformations, predominantly along the surface normal, at higher frequencies (4-8kHz), consistent with observations in dry skulls with both LDV systems (McKnight et al., 2013) and time-averaged holographic systems (Ogura, et al. 1979; Hoyer and Dörheide, 1983) . A complex motion was observed between 1 – 2 kHz possibly likely consisting of comparable amounts of RBM-like and local transverse deformation, indicating a “transition” frequency region, also shown by other research (Stenfelt and Goode, 2005 (a)). While the normal components are predominant at high frequencies, tangent components show local maxima with comparable or even equal magnitudes, suggesting a combination of bending and compression at the skull surface in some regions, with the combination of traveling waves, consistent with previous observations in dry skulls (Khalil et al., 1979), cadaver heads (Stenfelt, S. and Goode, 2005(a)), and live humans (Håkansson et al., 1994).

The use of intact cadaver heads in this study, prohibits the direct measurement of the relative motion between the outer and inner surface of the skull, which leaves an ambiguity in the distinction between skull bending and compression in the transverse (normal) direction relative to the skull surface. However, while previous research, with transient excitation on dry skulls (Trnka et al., 2004), have shown evidence of transverse (along the skull thickness) compression at the onset of the fast waves propagation, studies on the steady state dynamic response of the skull have shown no

significant differential motion between the inner and outer surface of dry skulls (McKnight et al., 2013), suggesting predominantly bending motion.

The phase maps of the 3D motion data (figure 7) indicates rigid-body-like motion pattern, consisting of both of translational and rotational components, at low frequencies (<1 kHz) and local deformations with travelling waves above 2 kHz. The traveling wave pattern is predominant in the surface normal component (transverse waves), but it is also visible in the tangent components (compressional waves), but with 7-10 dB lower magnitudes of skull deformation. The lower spatial resolution of the 3D measurements, with 25 mm pitch of the measurement point grid versus 5 mm pitch for the SLDV, makes for a more difficult wave speed estimation, based on the method described in section 2.4. However, the average spatial slopes (30-50 deg/cm) of the phase maps at 4 kHz indicate corresponding wave speed in the order of 500-700 m/s, which is comparable to estimates of 450-500 m/s from the 1D SLDV data and the 250-400 m/s reported in literature (Khalil et al., 1979; Håkansson et al., 1994; Tonndof and Jahn, 1981). It should be noted that the propagation velocity, for bending waves in shell-like structures (as the measured area of the superior section of the cranial vault), is dependent on multiple parameters, including but not limited to excitation frequency, thickness, structure and material properties of the bone, thus it could vary between specimens. This could account for some of the variability in the estimates for propagation speed based on the 1D SLDV and 3D LDV data in this study and other studies.

4.4 Individual and combined contribution of all motion components

Overall, the data in the intrinsic coordinate frame has similar values (within 3-5 dB) and spatial distribution as in the LDV frame, which is due to the low variation (less than ±20 deg) of angle between the surface normal and the optical axis (Z-axis) of the LDV across the measurement area. Analogically, the magnitude and phase pattern at high frequencies (4-8 kHz) is similar between the 3D LDV and SLDV, due to the predominant surface normal component of motion. However, the two measurement methods show significant differences (10-15 dB) at low frequencies (< 1 kHz), particularly between the combined motion of the skull based on the 3D velocity data and the SLDV motion

component (equivalent to Z-axis component of the 3D LDV), due to the significant tangent motion component, which is not captured by the 1D SLDV system.

Spatial motion data (Figure 8) for all cadaver heads and conditions (i.e., skin covered, perforated skin, bare skull) indicate 5-10 dB higher motion in the tangent directions, indicated by V_T, at frequencies of 500 Hz and lower, in agreement with the RBM fit indicating a predominant V_X component, approximately aligned with the surface tangent. At frequencies above 1kHz the motion component V_η, along the normal direction, becomes predominant (3-5 dB higher). However, while lower, the contribution of the combined tangent component V_T at the higher frequencies is comparable to the normal component V_η, which is indicative of spatially complex non-rigid body motion, consistent with local deformations (bending), and a combination of transverse and compression traveling waves.

The cross-over ("transition") frequency (Stenfelt, 2011), at which the transition between the two modes of vibration occurs, is estimated at around 500-800Hz (based on Figure 8), which is consistent with previous findings based on measurements of both dry (Khalil et al., 1979; McKnight et al., 2013) and gel-filled skulls (Franke, 1956). It can be also noticed that the cross over frequency (~500Hz) for skin covered Head 4 (Figure 8 Left) is lower than for the case of Head 4 with punctured skin (700 - 800Hz, or bare skull Head 4 and Head 5, indicating a possible effect of the skin at the measurement point, providing additional vibrational mass. This is consistent with the impedance dominated resonance frequency of the skull at 400Hz and the global skull resonance at 800-1000Hz described in (Stenfelt, 2011). The decrease of the cross-over frequency could also be explained with the increase of the effective vibrational mass due to the skin, as indicated in previous studies comparing motions of a gel-filled versus dry skull (Franke, 1956). However, the precise and definite estimation of the cross-over frequency and its dependence on the cadaver head condition would require measurements at more frequencies and more samples that in the current study. Overall, the skin surface motion components (Figure 8 Left) show a flatter (smoother) frequency response than the skull surface motion components, possibly due to higher material damping of the skin relative to the skull bone (Tjellström et al., 1980).

5 Conclusions

The results of this study show that regardless of the stimulation location, namely at mastoid or forehead, the mode of sound propagation from the Baha transducer across the skull is primarily as a rigid-body-like motion of the whole skull at low frequencies, and as traveling waves, resulting in local transverse (along the surface normal) deformation of the skull surface, at high frequencies (> 4 kHz). Sound propagation for stimulation with Baha transducer attached via steel headband is similar to that for attachment via implanted screw, provided that the corresponding applied forces are calibrated for.

The 3D velocity measurements confirmed the complex spatial and frequency dependence of the response of the cadaver heads indicated by the 1D data from the scanning LDV system for measurements on the bone and on the skin covering the bone. A higher resolution for 3D velocity measurements is desirable to get a more comprehensive understanding of spatial motion of the head due to bone conducted sound.

References

1. Brummund, M.K., Sgard, F., Petit, Y. and Laville, F., 2014. Three-dimensional finite element modeling of the human external ear: Simulation study of the bone conduction occlusion effect a. *JASA*, *135*(3), pp.1433-1444.
2. Dobrev, I., Stenfelt, S., Röösli, C., Bolt, L., Pfiffner, F., Gerig, R., Huber, A. and Sim, J.H., 2016. Influence of stimulation position on the sensitivity for bone conduction hearing aids without skin penetration. *IJA*, *55*(8), pp.439-446.
3. Eeg-Olofsson, M., Stenfelt, S., Håkansson, B., Taghavi, H., Reinfeldt, S., Östli, P. and Granström, G., 2011. Optimal position of a new bone conduction implant. *Cochlear implants international*, *12*(sup1), pp.S136-S138.
4. Franke, E.K., 1956. Response of the human skull to mechanical vibrations. *JASA*, *28*(6), pp.1277-1284.
5. Håkansson, B., Brandt, A., Carlsson, P. and Tjellström, A., 1994. Resonance frequencies of the human skull in vivo. *JASA*, *95*(3), pp.1474-1481.
6. Håkansson, B., Reinfeldt, S., Eeg-Olofsson, M., Östli, P., Taghavi, H., Adler, J., Gabrielsson, J., Stenfelt, S. and Granström, G., 2010. A novel bone conduction implant (BCI): engineering aspects and pre-clinical studies. *IJA*, 49(3), pp.203-215.
7. Homma, K., Shimizu, Y., Kim, N., Du, Y. and Puria, S., 2010. Effects of ear-canal pressurization on middle-ear bone-and air-conduction responses. *Hear. Res.*, 263(1), pp.204-215.
8. Hood, J.D., 1960. The principles and practice of bone conduction audiometry: A review of the present position. *The Laryngoscope*, *70*(9), pp.1211-1228.
9. Hoyer, H.E. and Dorheide, J., 1983. A study of human head vibrations using time-averaged holography. *J. Neurosurg.*, *58*(5), pp.729-733.
10. Hurley, R.M. and Berger, K.W., 1970. Relationship between vibrator placement and bone conduction measurements with monaurally deaf subjects. *JAR*, *10*(2), pp.147-150.

11. Ito, T., Röösli, C., Kim, C.J., Sim, J.H., Huber, A.M. and Probst, R., 2011. Bone conduction thresholds and skull vibration measured on the teeth during stimulation at different sites on the human head. *Audiol. & Neurotol.*, *16*(1), pp.12-22.
12. Khaleghi, M., Furlong, C., Ravicz, M., Cheng, J.T. and Rosowski, J.J., 2015. Three-dimensional vibrometry of the human eardrum with stroboscopic lensless digital holography. *J Biomed. Opt.*, *20*(5), pp.051028-051028.
13. Khalil, T.B., Viano, D.C. and Smith, D.L., 1979. Experimental analysis of the vibrational characteristics of the human skull. *JSV*, *63*(3), pp.351-376.
14. Kim, N., Homma, K. and Puria, S., 2011. Inertial bone conduction: symmetric and anti-symmetric components. *JARO*, 12(3), pp.261-279.
15. McKnight, C.L., Doman, D.A., Brown, J.A., Bance, M. and Adamson, R.B., 2013. Direct measurement of the wavelength of sound waves in the human skull. *JASA*, *133*(1), pp.136-145.
16. Nolan, M. and Lyon, D.J., 1981. Transcranial attenuation in bone conduction audiometry. *JLO,* 95(06), pp.597-608.
17. Ogura, Y., Masuda, Y., Miki, M., Takeda, T., Watanabe, S., Ogawara, T., Shibata, S., Uyemura, T. and Yamamoto, Y., 1979. Vibration analysis of the human skull and auditory ossicles by holographic interferometry. In *Holography in Medicine and Biology* (pp. 218-222). Springer Berlin Heidelberg.
18. Rodriguez, O., 1840. Des lois geometriques qui regissent les desplacements d'un systeme solide dans l'espace et de la variation des coordonnees provenant de deplacements consideres independamment des causes qui peuvent les produire. J Math Pure Appl., 5, pp.380-440.
19. Röösli, C., Dobrev, I., Sim, J.H., Gerig, R., Pfiffner, F., Stenfelt, S. and Huber, A.M., 2016. Intracranial pressure and promontory vibration with soft tissue stimulation in cadaveric human whole heads. *Otol. & Neurotol.*, 37(9), pp.e384-e390.
20. Sim, J.H., Chatzimichalis, M., Lauxmann, M., Röösli, C., Eiber, A. and Huber, A.M., 2010. Complex stapes motions in human ears. *JARO*, *11*(3), pp.329-341.

21. Sim, J.H., Dobrev, I., Gerig, R., Pfiffner, F., Stenfelt, S., Huber, A.M. and Röösli, C., 2016. Interaction between osseous and non-osseous vibratory stimulation of the human cadaveric head. *Hear. Res.*, *340*, pp.153-160. (doi: 10.1016/j.heares.2016.01.013)
22. Snyder, J.M., 1973. Interaural attenuation characteristics in audiometry. *The Laryngoscope*, *83*(11), pp.1847-1855.
23. Sohmer, H., Freeman, S., Geal-Dor, M., Adelman, C. and Savion, I., 2000. Bone conduction experiments in humans–a fluid pathway from bone to ear. *Hear. Res.*, *146*(1), pp.81-88.
24. Sohmer, H. and Freeman, S., 2004. Further evidence for a fluid pathway during bone conduction auditory stimulation. *Hear. Res.*, *193*(1), pp.105-110.
25. Steiner, L.A. and Andrews, P.J.D., 2006. Monitoring the injured brain: ICP and CBF. *Br. J. Anaesth., 97*(1), pp.26-38.
26. Stenfelt, S.P. and Håkansson, B.E., 1999. Sensitivity to bone-conducted sound: excitation of the mastoid vs the teeth. *Scand. Audiol.*, *28*(3), pp.190-198.
27. Stenfelt, S., Hato, N. and Goode, R.L., 2002. Factors contributing to bone conduction: the middle ear. *JASA*, *111*(2), pp.947-959.
28. Stenfelt, S., Wild, T., Hato, N. and Goode, R.L., 2003. Factors contributing to bone conduction: The outer ear. *JASA*, *113*(2), pp.902-913.
29. Stenfelt, S. and Goode, R.L., 2005 (a). Transmission properties of bone conducted sound: measurements in cadaver heads. *JASA*, 118(4), pp.2373-2391.
30. Stenfelt, S. and Goode, R.L., 2005 (b). Bone-conducted sound: physiological and clinical aspects. *Otol. & Neurotol.*, *26*(6), pp.1245-1261.
31. Stenfelt, S., 2006. Middle ear ossicles motion at hearing thresholds with air conduction and bone conduction stimulation. *JASA*, 119(5), pp.2848-2858.
32. Stenfelt, S., 2011. Acoustic and physiologic aspects of bone conduction hearing. In *Implantable Bone Conduction Hearing Aids* (Vol. 71, pp. 10-21). Karger Publishers.

33. Stenfelt, S., 2012. Transcranial attenuation of bone-conducted sound when stimulation is at the mastoid and at the bone conduction hearing aid position. *Otol. & Neurotol.*, *33*(2), pp.105-114.
34. Stenfelt, S., 2014. Inner ear contribution to bone conduction hearing in the human. *Hear. Res.*, 329, pp.41-51.
35. Stenfelt, S., 2016. Model predictions for bone conduction perception in the human. *Hear. Res.*, *340*, pp.135-143.
36. Studebaker, G.A., 1964. Clinical masking of air-and bone-conducted stimuli. *JSHD*, *29*(1), pp.23-35.
37. Thiel, W., 1992. Die Konservierung ganzer leichen in natürlichen farben. *Ann. Anat.*, *174*(3), pp.185-195.
38. Tjellström, A., Håkansson, B., Lindström, J., Brånemark, P.I., Hallen, O., Rosenhall, U. and Leijon, A., 1980. Analysis of the mechanical impedance of bone-anchored hearing aids. *Acta Otolaryngol.*, *89*(1-2), pp.85-92.
39. Tonndorf, J., 1966. Bone conduction. Studies in experimental animals. *Acta Otolaryngol.*, pp.Suppl-213.
40. Tonndorf, J. and Jahn, A.F., 1981. Velocity of propagation of bone-conducted sound in a human head. *JASA*, *70*(5), pp.1294-1297.
41. Trnka, J., Veselý, E. and Dvoráková, P., 2004. A study of wave propagation in a human skull using laser interferometry. *Exp. Tech.*, *28*(1), pp.27-30.
42. Von Békésy, Georg, 1960. Experiments in hearing. Edited by Ernest Glen Wever. Vol. 8. New York: McGraw-Hill.

Tables

Table 1. Overview of LDV measurement types, locations, and corresponding stimulation conditions for each cadaver head used in this study. Abbreviations within the table: IM = implant (screw); HB = 5N steel headband; S = skin; PS = perforated skin; B = bone

LDV type	1D					3D		
Baha® location	Mastoid			Forehead		Mastoid		
Baha® connection	IM		HB	IM	HB	IM		
Measurement surface	B	S	S	S	S	S	PS	B
Head 1	■							
Head 2		■	■	■	■			
Head 3		■		■				
Head 4						■	■	■
Head 5								■

Figure Captions

Figure 1. *A) Block diagram of the measurement system. B) Measurement grid at the superior part of the skull. Inter-position distance for the scanning LDV were about 5 mm, while measurement points for the 3D LDV were about 25 mm apart, both covering an area of approximately 100×100mm.*

Figure 2. *Illustration of the geometrical nomenclature used for the definition and calculation of: A) and B) surface wave speed based on the estimated distance between two consecutive nodes in the phase maps; C) tangent and normal motion components within an intrinsic coordinate system defined based on the local surface normal at each measurement point.*

Figure 3. *Mechanical impedance (in units of force/stimulus velocity) of the artificial mastoid (left), used for calibration of the output force of the Baha transducer in direct contact with the skin and supported by a steel head band (right). Corresponding force output data for screw supported Baha transducer, calibrated via a skull simulator TU-1000, is included for comparison.*

Figure 4. *Velocity response (admittance) of surface of the bone of Head 1(leftmost column), and skin of Head 2 (2nd column from left), and Head 3 (3rd column from left) to stimulation with a Baha transducer attached via screw at the mastoid. Rightmost column shows the RBM fit for Head 3 with corresponding average normalized RBM fit difference* Δv_r. *Included are the magnitude and phase of the response for stimulation at low (0.5-1kHz), medium (2kHz) and high (6-8kHz) frequencies. Direction of propagation of traveling waves at 6-8kHz are indicated in the phase maps. Color mapping, for the magnitude data is in logarithmic scale with 0 dB = 1 mm/s/N. Corresponding color bars indicate ±2 standard deviations from the data mean at each stimulation frequency. Color mapping for the phase data is in linear scale in the range of -180 to 180 deg. Spatial*

axis units are mm. Approximate location of the stimulation position is marked with a circle in the lowest panels.

Figure 5. *Velocity response of the surface of the skin of Head 2 to stimulation with a Baha transducer attached via screw or headband at the mastoid. Included are the magnitude and phase of the response for stimulation at 0.5 kHz (top row), 2 kHz (middle row) and 8 kHz (bottom row). Indicated is the corresponding average normalized RBM fit difference* Δv_r*. Directions of wave propagation at 8 kHz are indicated in the phase maps. Color mapping, for the magnitude data is in logarithmic scale such that 0 dB = 1 mm/s/N. The color bars ranges ±2 standard deviations of the mean at each frequency. Spatial axis units are mm. Color mapping for the phase data is in linear scale in the range of -180 to 180 deg. Approximate location of the stimulation position is marked with a circle.*

Figure 6. *Velocity response of surface of the skin of Head 2 to stimulation with a Baha transducer attached via screw or headband at the forehead. Included are the magnitude and phase of the response for stimulation at 0.5kHz (top row), 2kHz (middle row) and 8kHz (bottom row). Direction of propagation of traveling waves at 8kHz are indicated in the phase maps. Indicated is the corresponding average normalized RBM fit difference* Δv_r*.Color mapping of the magnitude maps is in logarithmic scale such that 0dB = 1mm/s/N. Corresponding color bars indicate ±2σ (standard deviations) from the data mean at each stimulation frequency. Spatial axis units are mm. Color mapping for the phase data is in linear scale in the range of -180 to 180 deg. Approximate location of the stimulation position is marked with a circle.*

Figure 7. *All velocity components, expressed in both LDV and intrinsic coordinate systems, of the response of surface of the skull of Head 5, due to stimulation with a Baha transducer attached via a screw at the mastoid. Included are the magnitude and phase of the response for stimulation at 0.25 and 4kHz. Direction of propagation of traveling waves at 4kHz are indicated in the phase maps. Indicated on the right is the corresponding average normalized RBM fit difference* Δv_r*. Color mapping of the*

magnitude maps is in logarithmic scale such that 0dB = 1mm/s/N. Corresponding color bars are set to include approximately ±2σ (standard deviations) from the data mean at all stimulation frequencies. Color mapping for the phase data is in linear scale in the range of -180 to 180 deg. Approximate location of the stimulation position is marked with a circle. An illustration of the anatomical and LDV coordinate systems is included to aid the data interpretation.

Figure 8. *Relative contribution of normal and tangential motion components (left), and the difference between a RBM and the measured motion (right) for cadaver heads 4 (3 surface conditions) and 5, based on 3D LDV data.*

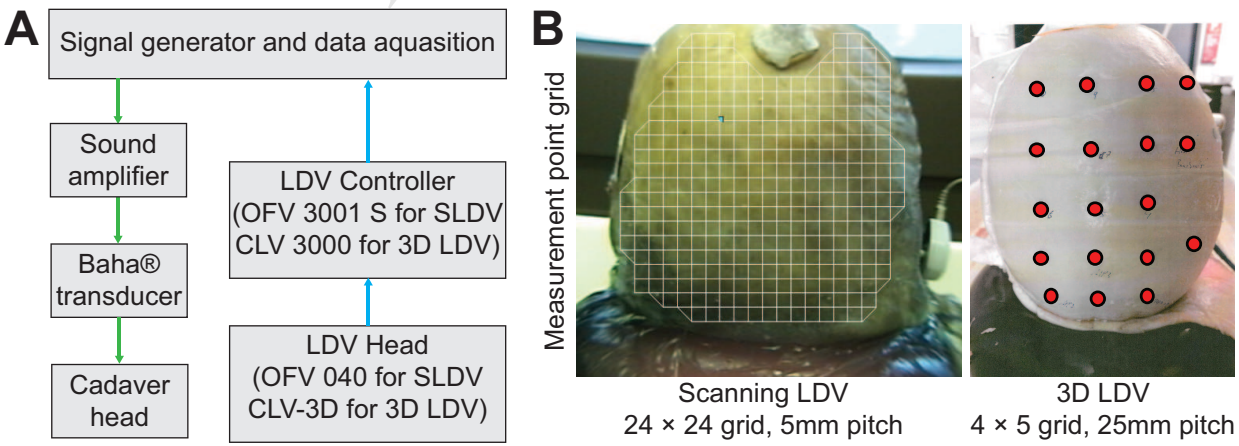

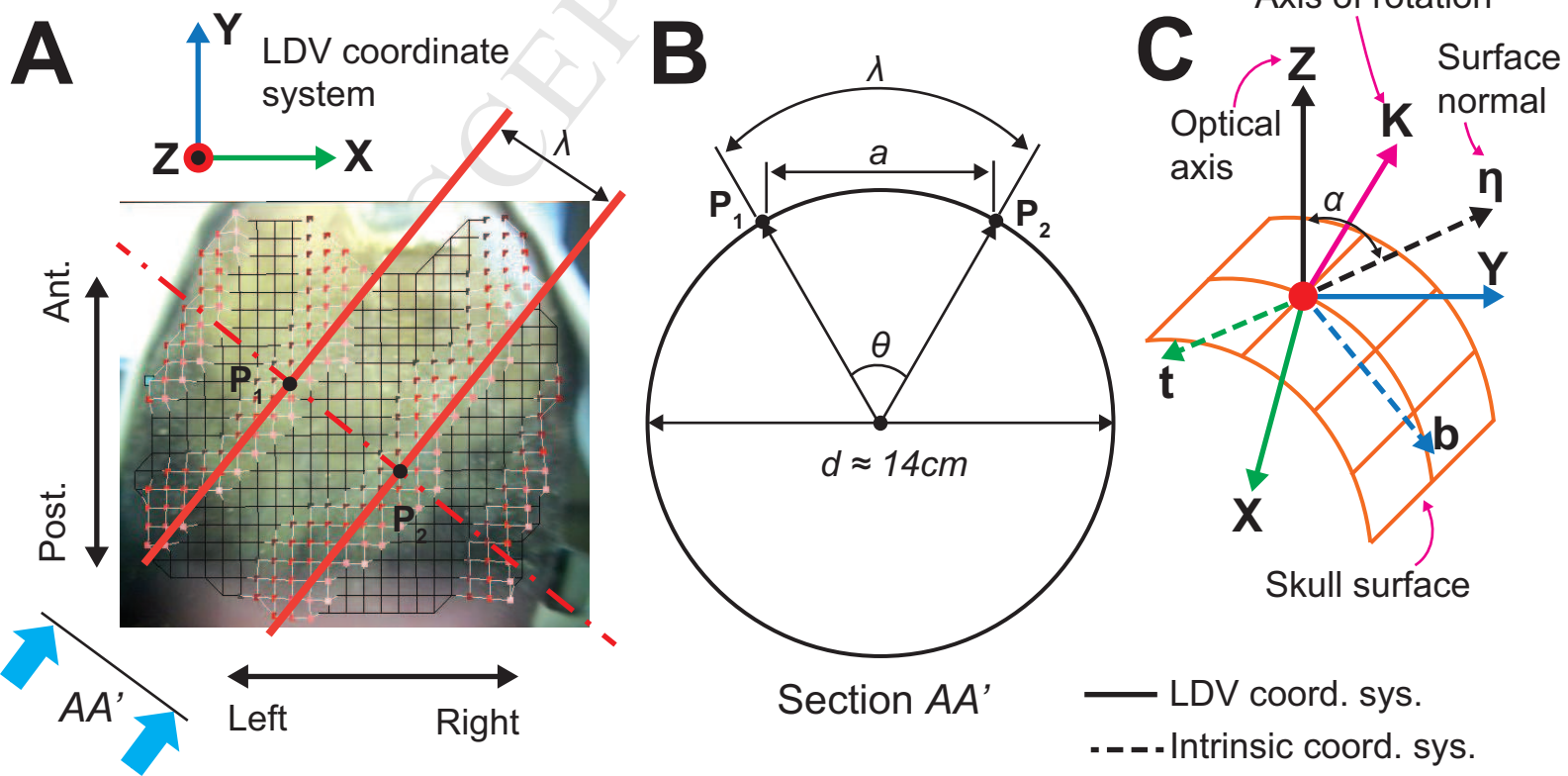

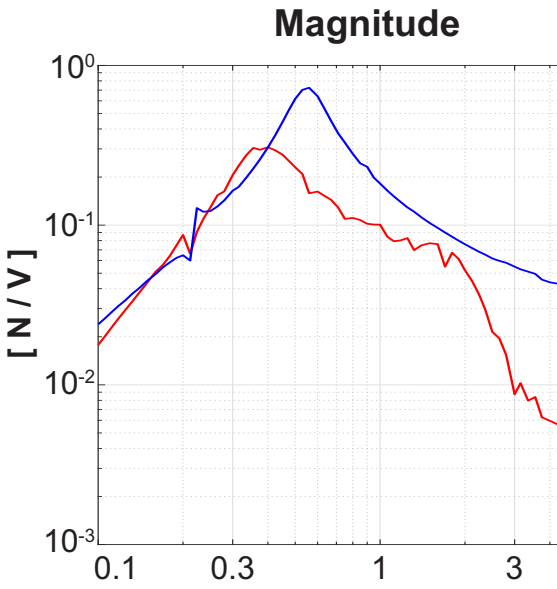

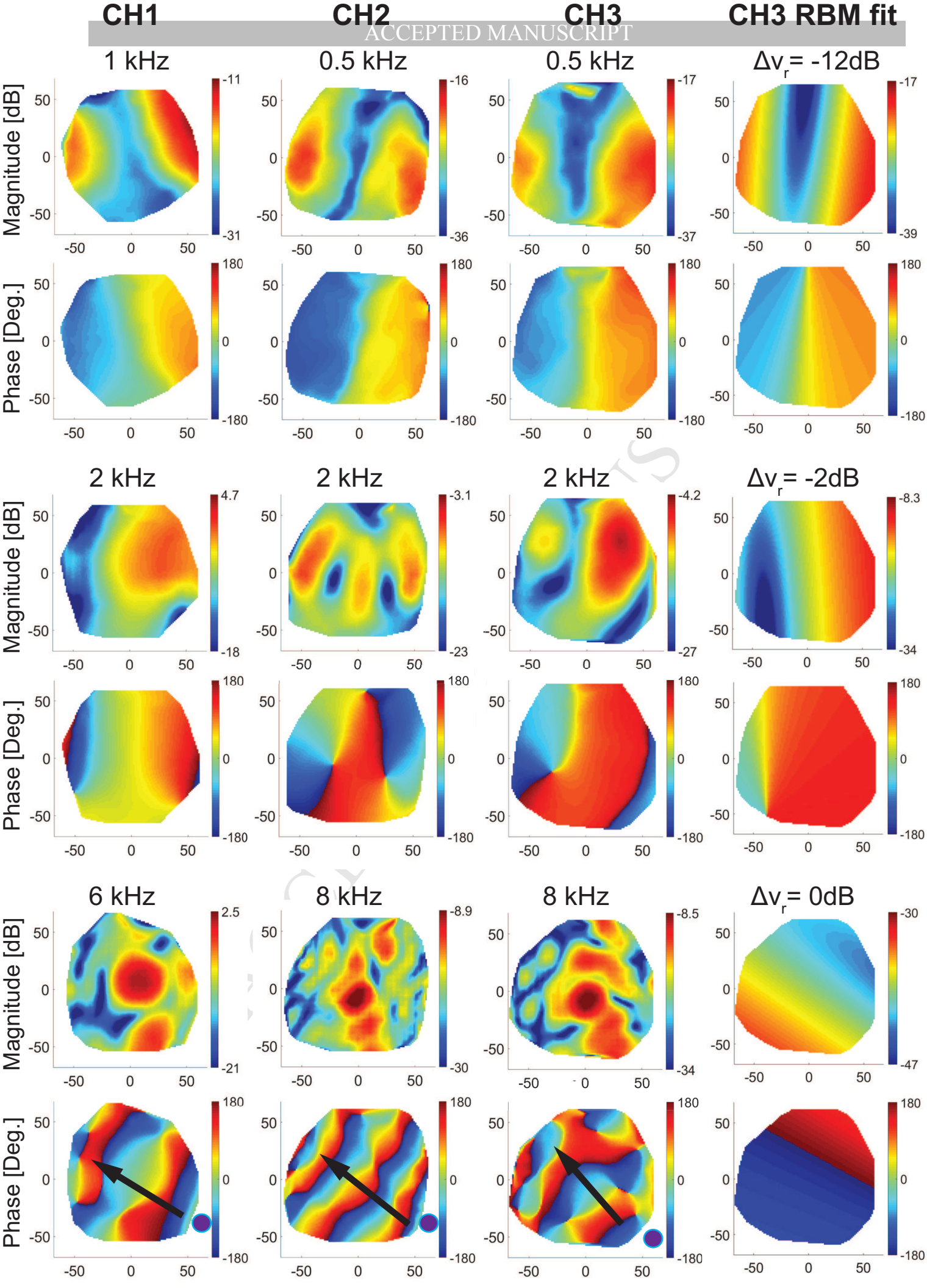

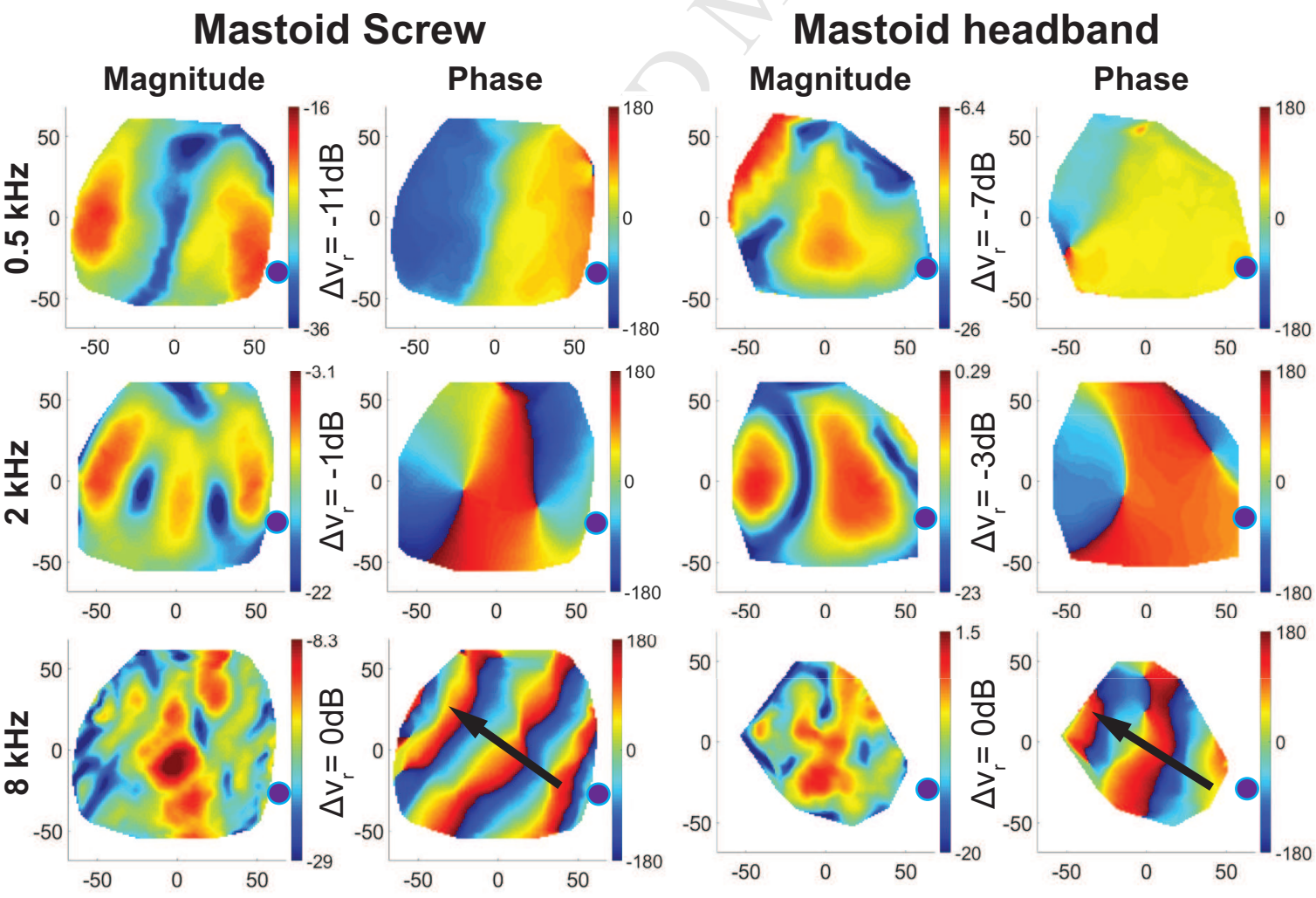
Mastoid Screw
Mastoid headband
Magnitude
Phase
Magnitude
Phase
0.5 kHz
2 kHz
8 kHz
Δv_r = -11dB
Δv_r = -7dB
Δv_r = -1dB
Δv_r = -3dB
Δv_r = 0dB
Δv_r = 0dB
-16
-36
180
0
-180
-6.4
-26
-3.1
-22
0.29
-23
-8.3
-29
1.5
-20
50
0
-50

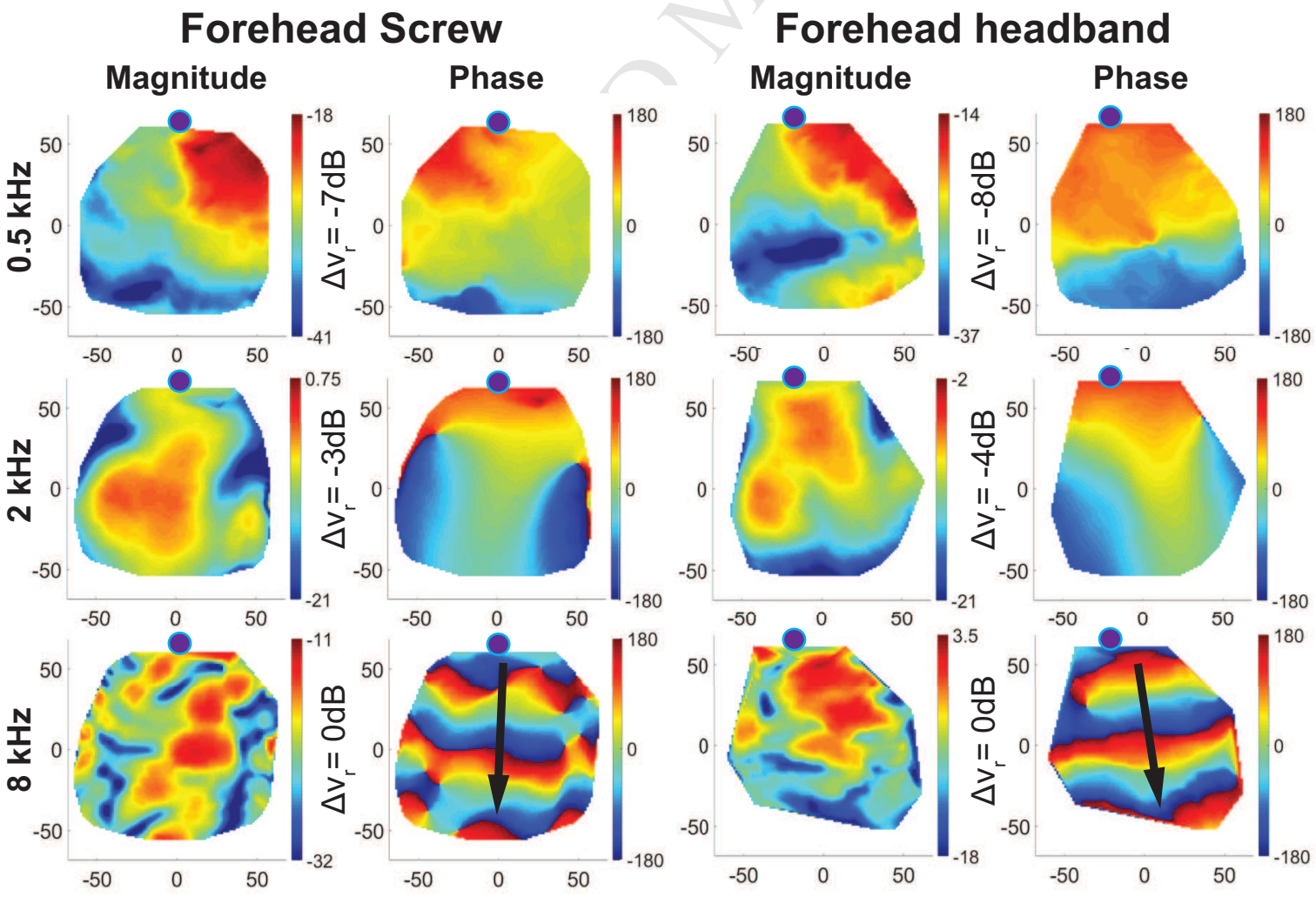
Forehead Screw
Forehead headband
Magnitude
Phase
Magnitude
Phase
0.5 kHz
2 kHz
8 kHz
Δv_r = -7dB
Δv_r = -8dB
Δv_r = -3dB
Δv_r = -4dB
Δv_r = 0dB
Δv_r = 0dB
-18
-41
180
-180
-14
-37
0.75
-21
-2
-11
-32
3.5
-18
50
0
-50

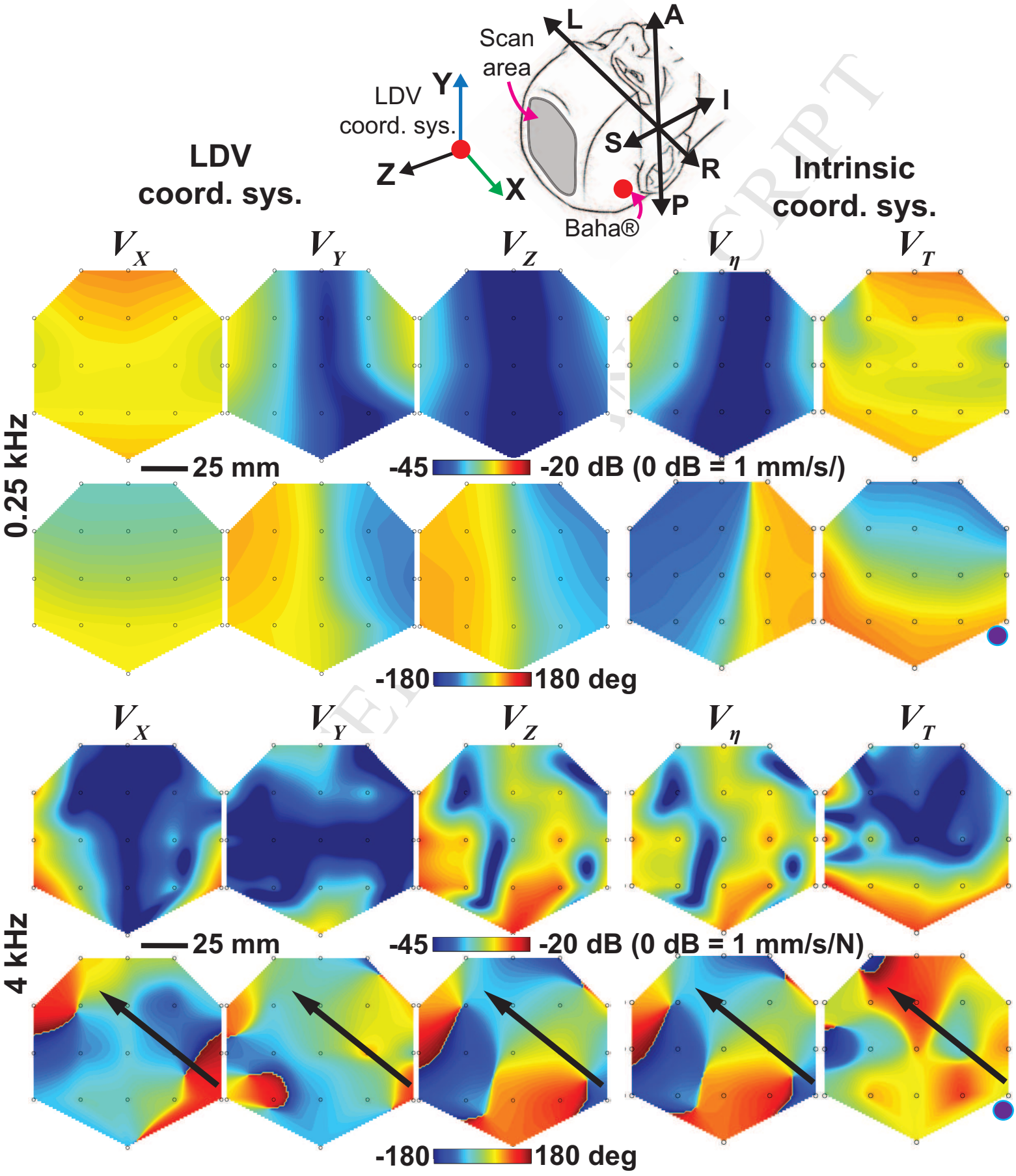
LDV
coord. sys.
Scan
area
LDV
coord. sys.
Y
Z
X
L
A
I
S
R
P
Baha®
Intrinsic
coord. sys.
V_X
V_Y
V_Z
V_η
V_T
0.25 kHz
25 mm
-45
-20 dB (0 dB = 1 mm/s/)
-180
180 deg
V_X
V_Y
V_Z
V_η
V_T
4 kHz
25 mm
-45
-20 dB (0 dB = 1 mm/s/N)
-180
180 deg

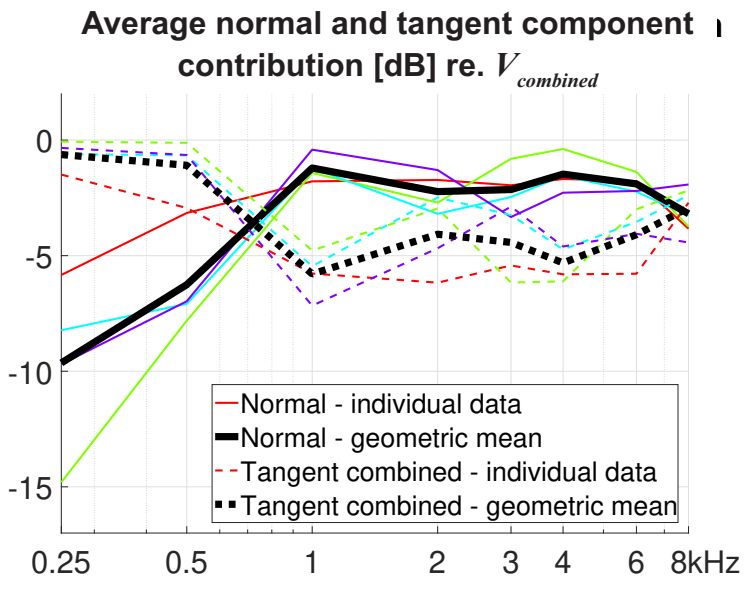
Average normal and tangent component contribution [dB] re. $V_{combined}$
0
-5
-10
-15
0.25
0.5
1
2
3
4
6
8kHz
Normal - individual data
Normal - geometric mean
Tangent combined - individual data
Tangent combined - geometric mean

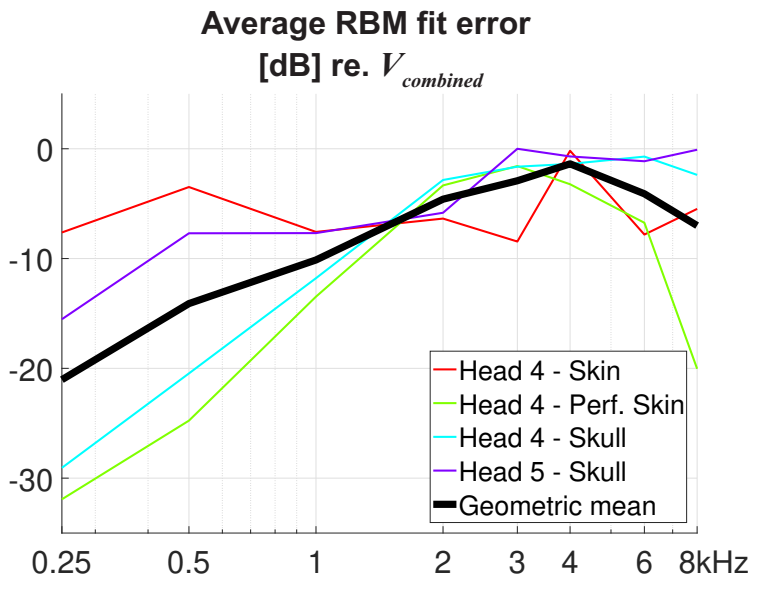
Average RBM fit error [dB] re. $V_{combined}$
0
-10
-20
-30
0.25
0.5
1
2
3
4
6
8kHz
Head 4 - Skin
Head 4 - Perf. Skin
Head 4 - Skull
Head 5 - Skull
Geometric mean

Research Highlights

- Demonstrated methodologies to measure the full three-dimensional motion at a grid of points across the human cadaver heads.
- 3D Laser Doppler velocity measurements allow for analysis of the relative contribution of the tangent and normal motion components.
- Motions below 1 kHz are predominantly along the surface tangent plane and are similar to rigid body motion.
- Motions above 2 kHz are predominantly along the surface normal, consistent with local bending vibration modes